Nanoscale Advances

ROYAL SOCIETY OF CHEMISTRY

PAPER

View Article Online
View Journal | View Issue

Cite this: *Nanoscale Adv.*, 2022, **4**, 926

Toward efficient dye degradation and the bactericidal behavior of Mo-doped La_2O_3 nanostructures

Muhammad Ikram, †*[a] Namra Abid,†[b] Ali Haider,[c] Anwar Ul-Hamid,[d] Junaid Haider,[e] Anum Shahzadi,[f] Walid Nabgan,*[g] Souraya Goumri-Said,[h] Alvina Rafiq Butt[b] and Mohammed Benali Kanoun*[i]

In this study, different concentrations (0, 0.02, 0.04, and 0.06 wt%) of Mo doped onto La_2O_3 nanostructures were synthesized using a one-pot co-precipitation process. The aim was to study the ability of Mo-doped La_2O_3 samples to degrade toxic methylene blue dye in different pH media. The bactericidal potential of synthesized samples was also investigated. The structural properties of prepared samples were examined by XRD. The observed XRD spectrum of La_2O_3 showed a cubic and hexagonal structure, while no change was recorded in Mo-doped La_2O_3 samples. Doping with Mo improved the crystallinity of the samples. UV-Vis spectrophotometry and density functional theory calculations were used to assess the optical characteristics of Mo–La_2O_3. The band gap energy was reduced while the absorption spectra showed prominent peaks due to Mo doping. The HR-TEM results revealed the rod-like morphology of La_2O_3. The rod-like network appeared to become dense upon doping. A significant degradation of MB was confirmed with Mo; furthermore, the bactericidal activities against *S. aureus* and *E. coli* were measured as 5.05 mm and 5.45 mm inhibition zones, respectively, after doping with a high concentration (6%) of Mo.

Received 12th November 2021
Accepted 28th December 2021

DOI: 10.1039/d1na00802a

rsc.li/nanoscale-advances

1. Introduction

Environmental contamination spurred on by rapid industrialization and urbanization impacts human lives directly. Numerous industries, including leather, textiles, paper, rubber, plastic, cosmetics, and food, produce organic toxic dyes as waste products on a regular basis.[1–3] Industrial wastewater contains heavy metals and other inorganic (trace elements, mineral acids, sulfates, inorganic salts, metal complexes with organic compounds) and organic (phenols, dyes, polyaromatic hydrocarbons, pesticides, *etc.*) pollutants.[4,5] These contaminants endanger aquatic fauna and flora, as well as human health. Dyes, referred to as coloring agents, are organic substances that bind chemically to the fabric surface to produce color. A dye is highly discernible even in small concentrations (less than 1 ppm) and carries toxicologically dangerous effects. It is the most common pollutant in textile industrial wastewater. Methylene blue ($C_{16}H_{18}N_3SC$) is a cationic dye possessing a heterocyclic aromatic chemical composition that is extensively used for coloring cotton, wool, and silk. Approximately 40% of synthetic dyes, such as methylene blue, are poisonous, mutagenic, and carcinogenic substances that persist in industrial wastes and have the potential to become the source of several serious health and environmental health issues.[6–8] To reduce environmental waste, factories are regulated to transform their dye impurities into acceptable outcome before disposal.[9] Moreover, waste recovery processes should utilize water in a sustainable and cost-effective manner.[10] Catalysis, electrolysis, photocatalysis, ion exchange, carbon filtering, adsorption, chemical precipitation, nanofiltration, reverse osmosis, and microbial control are a few of the most often used industrial water removal techniques.[3,11–13] Among these, catalysis is a popular method because it is ecologically beneficial, cost-beneficial, and energy-efficient.[14] Mastitis is a significant economic burden on the dairy industry. It is accompanied by chemical, microbiological, and physical alterations in milk, and also pathological abnormalities in mammary gland structures.[15]

[a]*Solar Cell Application Research Lab, Department of Physics, Government College University Lahore, Lahore 54000, Punjab, Pakistan. E-mail: dr.muhammadikram@gcu.edu.pk*

[b]*Physics Department, Lahore Garrison University, Lahore 54000, Punjab, Pakistan*

[c]*Faculty of Veterinary and Animal Sciences, Muhammad Nawaz Shareef University of Agriculture, 66000, Multan, Pakistan*

[d]*Core Research Facilities, King Fahd University of Petroleum & Minerals, Dhahran 31261, Saudi Arabia*

[e]*Tianjin Institute of Industrial Biotechnology, Chinese Academy of Sciences, Tianjin 300308, China*

[f]*Faculty of Pharmacy, University of the Lahore, Lahore, Pakistan*

[g]*School of Chemical and Energy Engineering, Faculty of Engineering, Universiti Teknologi Malaysia, 81310 Skudai, Johor, Malaysia. E-mail: wnabgan@gmail.com*

[h]*College of Science, Physics Department, Alfaisal University, P.O. Box 50927, Riyadh 11533, Saudi Arabia*

[i]*Department of Physics, College of Science, King Faisal University, P.O. Box 400, Al-Ahsa, 31982, Saudi Arabia. E-mail: mkanoun@kfu.edu.sa*

† M. Ikram and N. Abid are equal contributors.

Mastitis is caused by infectious agents, including bacteria, viruses, and fungi. The most common bacteria pathogens are *Coliform* and *Staphylococcus aureus*.[16,17] Multiple drug-resistant Gram-positive and Gram-negative bacterial species have emerged in recent years, posing a substantial risk to public health.[18,19]

The discovery of nanomaterials has revolutionized dye-contaminated wastewater treatment technologies. Small nanostructures in the size range between 1 and 100 nm possess remarkable surface-to-volume ratios compared to the bulk chemical composition, instigating significant improvements in chemical (biological, catalytic activity, *etc.*) and physical properties.[20,21] A considerably large number of metal oxides (MOs) are employed to degrade several organic impurities found in industrial wastewater. Nano-sized metallic oxides have a large number of industrial and technological applications, including environmental, optical, and mechanical gadgets.[22–24] MOs such as ZnO, TiO_2, La_2O_3, CeO_2, and so forth are utilized for dye degradation.[25–29] Among the alluring and potentially beneficial rare-earth MOs is La_2O_3 which has an energy gap of 4.3–5.8 eV.[30,31] Due to the rare electronic configuration [4f electrons] in lanthanides, their applications have been reported in diverse fields.[32,33] La_2O_3 has properties that set it apart from the other oxides in the series, due to the fact that La^{3+} is the only trivalent cation among the rare-earth elements without 4f electrons and possesses a simple xenon-like electronic structure.[34] Rare-earth elements have anticoagulant, antiemetic, bactericidal, antitumor, and anticancer effects. They have sparked a lot of attention in medicine and pharmacology. Rare-earth metals are well known for their antioxidant and antibacterial properties in animals.[35,36] Lanthanum-containing inorganic compounds are less expensive than the rest of the rare-earth host materials (Y_2O_3, Gd_2O_3, *etc.*).[37] La_2O_3 has been used in numerous applications, such as H_2 storage materials, superconductors, optoelectronic gadgets, laser crystals, LEDs, biosensors, excessive refraction optical fibers, and catalysts.[30–33,38] Additionally, as a basic element, lanthanum's oxides and hydroxides can react with CO_2 in the air to generate a less crystalline carbonate.[39] For the synthesis of La_2O_3 nanostructures, several approaches have been devised, including hydrothermal,[40] sol–gel,[41] thermal deposition,[42] co-precipitation,[34,43] and sonochemical,[32] as well as other physiochemical techniques. Among these, co-precipitation is the most convenient and economic method, as it does not require any specific equipment.[44] The application field and catalytic activity of synthesized La_2O_3 nanostructures have been shown to be highly influenced by the preparation procedure.[30,45]

Because of its thermal stability and distinctive electronic structure, Mo is a popular co-catalyst and helpful dopant among related elements.[46] It increases absorption in both the ultraviolet (UV) and visible light, and decreases the optical band gap. The Mo dopant may also increase the charge-carrier concentration. Studies have shown that Mo atoms can increase the metal oxide semiconductor stability and band structure.[47–49] In this work, undoped La_2O_3 and Mo (0.02, 0.04, and 0.06 wt%)-doped La_2O_3 nanostructures were effectively synthesized *via* a one-pot co-precipitation approach. The synthesized material was employed to remove the toxic dye MB. Its antibacterial

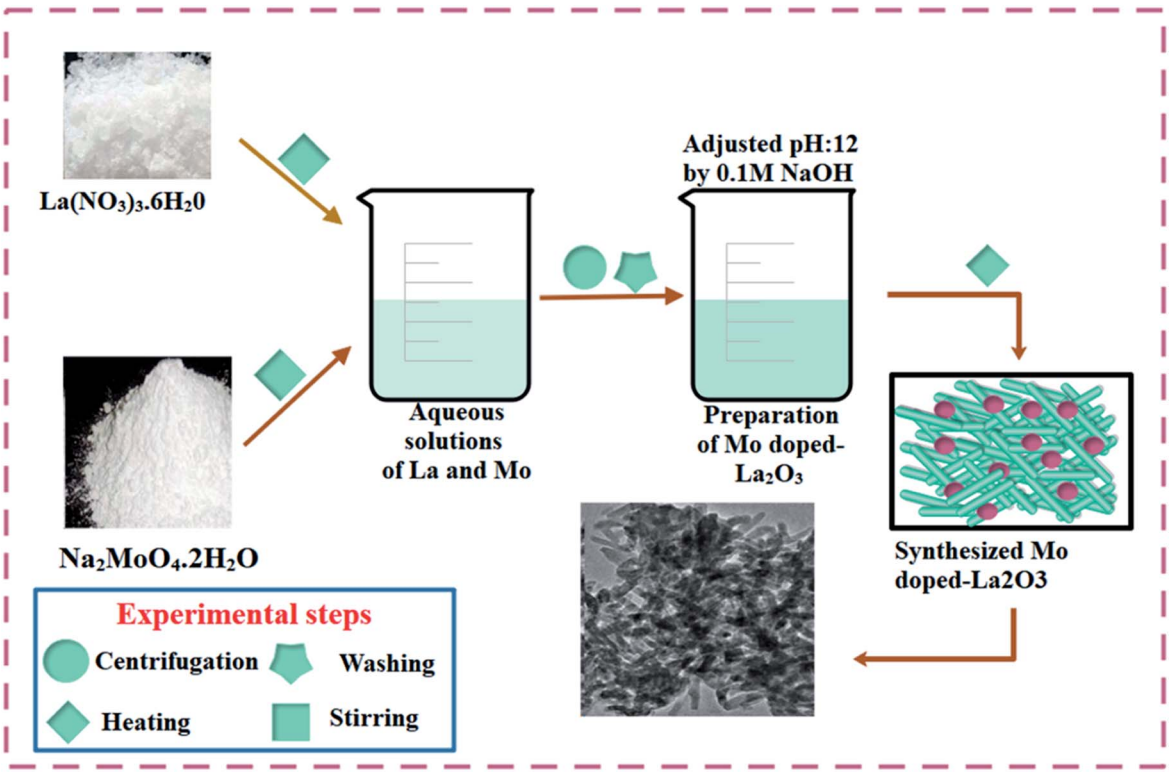

Fig. 1 Schematic diagram of the synthesis of the Mo–La_2O_3 nanostructures.

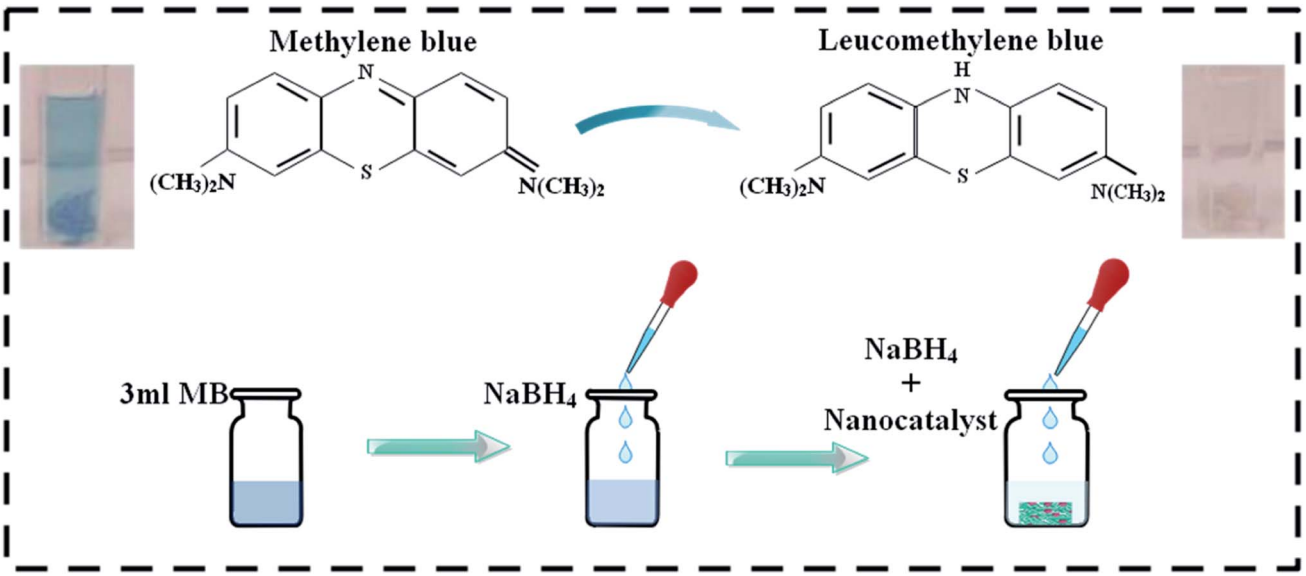

Fig. 2 Schematic diagram showing the experimental approach to evaluate the catalytic activity.

potential against *Escherichia coli* (*E. coli*) and *Staphylococcus aureus* (*S. aureus*) bacteria was also evaluated. Theoretical calculations were undertaken to reveal the change in the band gap (E_g) energy and optical properties with an increase in the Mo concentration.

2. Experimental section

2.1 Materials

Lanthanum nitrate hexahydrate ($La(NO_3)_3 \cdot 6H_2O$, >99%), sodium molybdate dihydrate ($Na_2MoO_4 \cdot 2H_2O$, 99%), and sodium hydroxide (NaOH, 98%) were procured from Sigma Aldrich (Germany).

2.2 Preparation of pure and Mo-doped La_2O_3 nanostructures

To prepare La_2O_3 nanostructures, 0.5 M of $La(NO_3)_3 \cdot 6H_2O$ was prepared under constant stirring at 80 °C for 30 min. The desired amount of NaOH was added dropwise into the stirred solution to maintain pH ~ 12, under stirring at 100 °C for 3 h. The precipitates were isolated by centrifuge at 7500 rpm. The precipitates were dried for 12 h at 150 °C and milled into a fine powder. The above-mentioned method was adopted for all the doped samples, whereby Mo-doped La_2O_3 was synthesized with various concentrations of Mo (0.02, 0.04, and 0.06 wt%). The synthesis route used is depicted schematically in Fig. 1.

2.3 Catalytic activity (CA)

The degradation of methylene blue MB (oxidizing agent) was used as a means to assess the catalytic activity of the dopant-free and doped La_2O_3 nanostructures in the presence of sodium borohydride $NaBH_4$ (reducing agent), with the prepared nanostructures acting as a catalyst in this study. To ensure the purity of the experiment, all the reagents, including MB and $NaBH_4$, were used immediately after preparation. First, 3 mL aqueous MB solution was combined with freshly prepared (400 μL) 0.1 M $NaBH_4$ solution followed by adding 400 μL Mo-doped nanostructures (0, 2, 4, and 6 wt%) to the solution. It is worth remembering that a catalyst reduces the reaction activation energy (E_a), thus improving its stability and rate. Adsorption occurs when a catalyst is incorporated into MB in the presence of a reducing agent. The decolorization and variation in dye absorption intensity over time can be used to assess the reaction rate (Fig. 2). The size of the particles influences the catalytic activity of the dye because smaller particles have a higher surface-to-volume ratio, resulting in enhanced catalytic activity. In analytical chemistry, the most widely used redox indicator to regulate catalytic activity during a dye degradation test is MB. Furthermore, when oxidized, MB appears blue, and when reduced, it appears neutral, as shown in Fig. 2.[50]

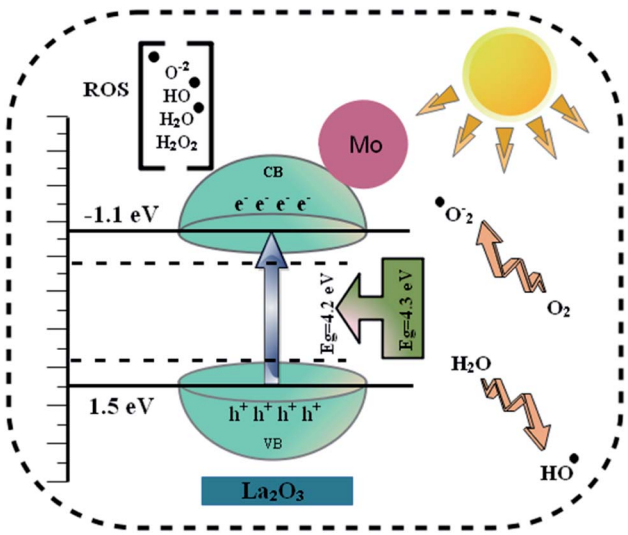

Fig. 3 Schematic illustration of the photocatalysis mechanism of the Mo-doped La_2O_3 nanostructures.

2.4 Photocatalytic activity (PCA)

The present study involved MB degradation in the presence of Mo-doped La_2O_3 nanostructures under sunlight. UV-Vis spectrophotometry was engaged to record the photocatalytic activity of all the concerned samples at room temperature. A stock solution of MB (g mL^{-1}) was prepared and 10 mg of synthesized samples was mixed with 30 mL stock solution. Before illumination, these samples were kept in the dark for 30 min to achieve a strong adsorption–desorption equilibrium between the MB and the photocatalyst. The solution was then transferred to a photoreactor after vigorous stirring. A Hg lamp (400 W, 20 cm) was used as the visible-light source. Afterward, 3 mL solution was separated for UV-Vis analysis at various time intervals. The maximum absorption (λ_{max}) for MB was attained at 665 nm for all the samples. The following equation was used to calculate the percentage (%) degradation:

$$\%\ \text{Degradation} = \frac{C_0 - C_t}{C_t} \times 100 \quad (1)$$

where C_0 and C_t are the initial and final concentrations of MB, respectively.

2.4.1 Reaction mechanism and kinetics. A possible PCA mechanism is depicted in Fig. 3. Photocatalytic degradation entails numerous processes, including adsorption–desorption, electron–hole pair formation, electron pair recombination, and chemical reaction.[51,52] The PCA begins with photoexcitation, which is initiated by photons processing energy equal to or more than the material band gap energy (E_g). These photons stimulate valence/lower band (VB) electrons, causing them to move to the conduction/higher band (CB). Electrons leave holes in the VB, resulting in the formation of $e–h^+$ pairs, as stated in the equation below.

$$La_2O_3 + h\nu \rightarrow e^-(CB) + h^+(VB) \quad (2)$$

The photon-induced electrons react with oxygen to form the superoxide radical $O_2^{\bullet -}$.

$$e^- + O_2 \rightarrow O_2^{\bullet -} \quad (3)$$

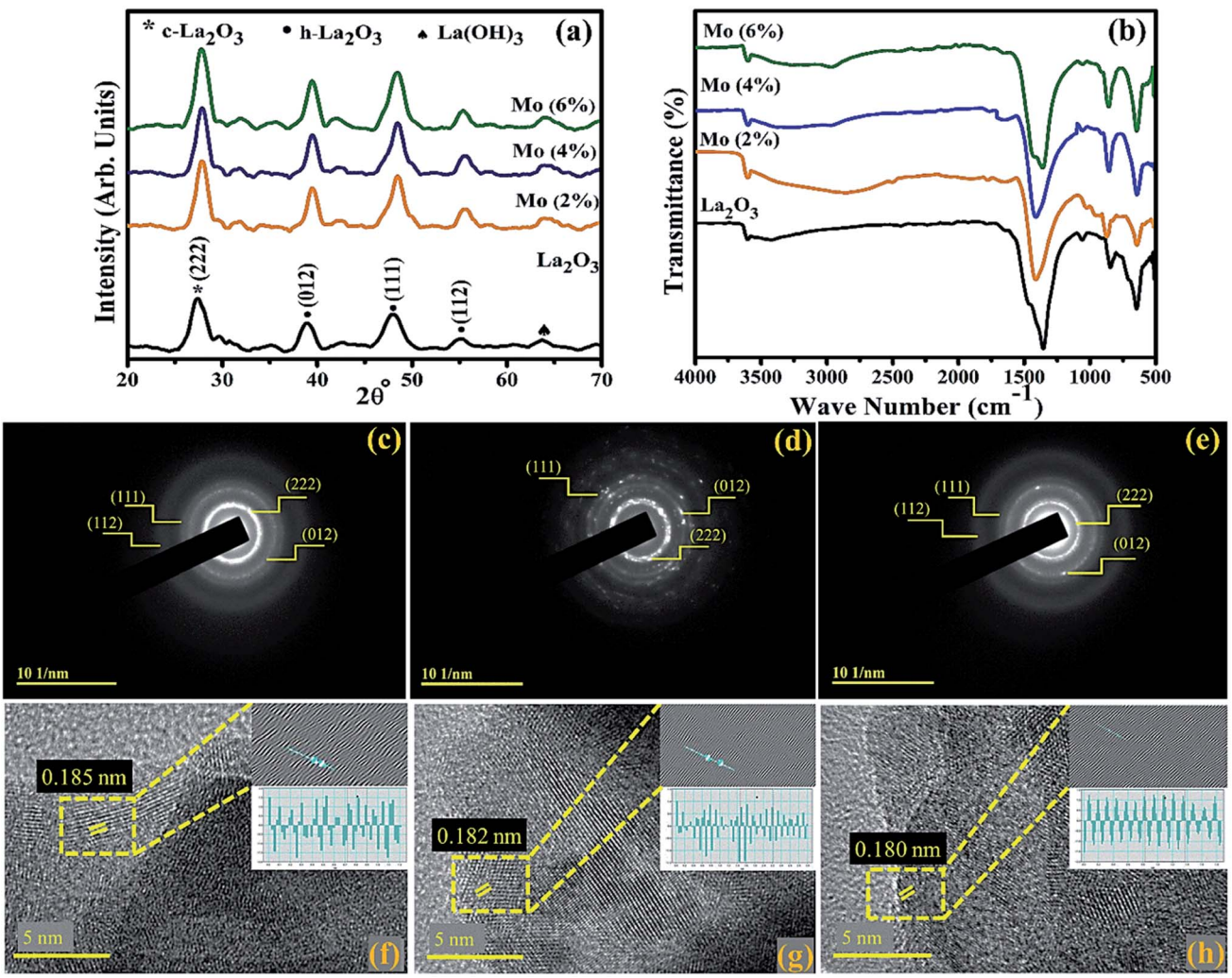

Fig. 4 (a) XRD patterns, (b) FTIR spectra of the synthesized samples, (c–e) SAED patterns, and (f–h) *d*-spacing of pristine and the 4% and 6% doped nanostructures.

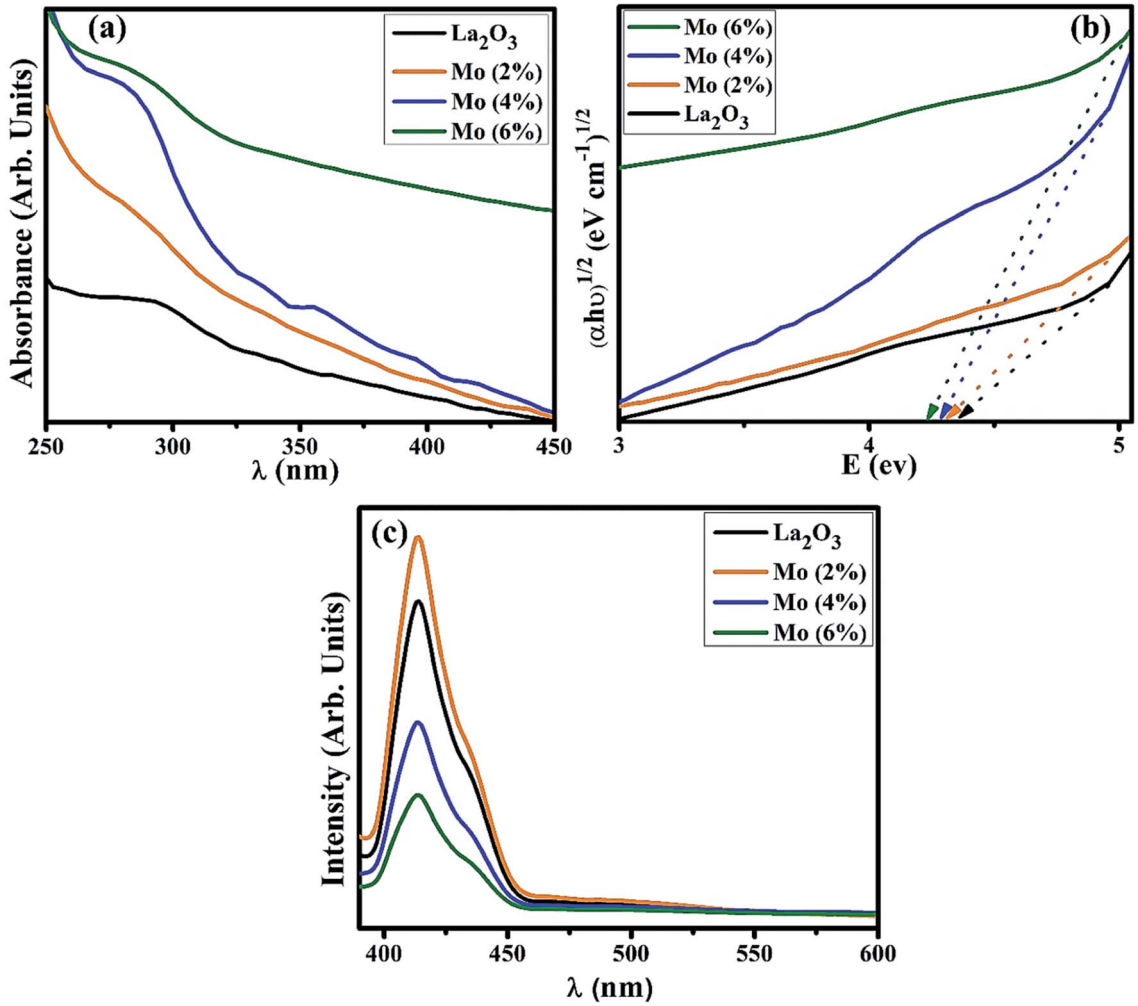

Fig. 5 (a) Absorption spectra, (b) band gap energy plot, (c) PL spectra of La_2O_3 and Mo-doped La_2O_3 nanostructures.

Later, when these superoxide radicals $O_2^{\bullet -}$ react with water, oxidizing agents, such as hydroperoxy ($HO_2^{\bullet}$) and hydroxyl radicals ($OH^{\bullet}$), are produced, which are crucial for the breakdown of organic contaminants.

$$O_2^{\bullet -} + H_2O \rightarrow HO_2^{\bullet} + OH \quad (4)$$

Water on the photocatalyst surface may also be trapped in these irradiation-induced holes, producing hydroxyl radicals ($OH^{\bullet}$).

$$h_{VB}^{+} + OH^{-} \rightarrow {}^{\bullet}OH_{ad} \quad (5)$$

$$h_{VB}^{+} + H_2O \rightarrow {}^{\bullet}OH + H^{+} \quad (6)$$

Finally, the oxidation of organic molecules produces CO_2 and H_2O.

$$^{\bullet}OH + \text{organic molecules} + O_2 \rightarrow \text{products } (CO_2 \text{ and } H_2O) \quad (7)$$

Furthermore, even a minor recombination of electron–hole pairs, which may be lost eventually, will affect the photocatalytic activity of the nanocatalyst.[53]

$$e_{CB}^{-} + h_{VB}^{+} \rightarrow La_2O_3 \quad (8)$$

2.5 Segregation and characterization of *S. aureus* and *E. coli*

Mastitis-positive ewe milk specimens from Punjab animal hospitals and farms were cultured using 5% blood agar (SBA). Overnight incubation at 37 °C proceeded and the resulting bacteria were purified by streaking in triplicate on MacConkey (MA) and mannitol salt agar (MSA) at pH ~ 7. Coagulation, catalase, and Gram staining were used to distinguish the extracted commodities biochemically and morphologically.

2.6 Antimicrobial activity

To evaluate the bactericidal capabilities of Mo-doped La_2O_3 nanostructures, Gram-positive (*S. aureus*) and Gram-negative (*E. coli*) microbes were recovered effectively from ovine mastitic fluid. The bactericidal content was assessed *in vitro* by swabbing *S. aureus* and *E. coli* strains on MSA and MA, correspondingly. Bacterial remedies containing 0.5 Mc-Farland standard were swabbed onto agar plates, while wells 6 mm wide were formed

using a sterile cork borer. In comparison to ciprofloxacin (5 μg/50 μL) used as a standard drug and DIW (50 μL) used as a negative control, the wells were filled with distinct concentrations of the doped nanomaterial, *e.g.*, 500 and 1000 μg/50 μL. The sensitivity of all the generated samples was determined using a Vernier caliper after 24 h incubation (37 °C) of the agar dishes. To assess the antibacterial effect, one-way analysis of variance was employed.

2.7 Characterization

A PANalytical XPert PRO X-ray diffraction (XRD) system employing Cu Kα radiation ($\lambda \sim 0.0154$ nm) was utilized to determine the crystal structure and phase information of the nanostructures in the 2θ range from 20° to 70°. A PerkinElmer spectroscope was used to detect the presence of functional groups from the FTIR spectra. A UV-Vis spectrophotometer (Genesys 10S) was employed to examine the optical properties in the range from 200 to 700 nm. The samples' morphologies and microstructures were recorded with a JSM-6460LV FE-SEM system coupled with an EDX spectrometer. PL spectra were obtained on a JASCO FP-8300 system for the pure and doped La_2O_3. The HR-TEM equipment JEOL JEM 2100F was used to measure the inter-planner *d*-spacing of the prepared nanostructures.

2.8 Computational details

First-principles computation based on the framework of density functional theory (DFT) within the Perdew, Burke, Ernzerhof (PBE) for the exchange–correlation functional[54] were carried out using the Quantum Atomistix ToolKit (QuantumATK) package.[55] Norm-conserving PseudoDojo pseudopotentials were used to describe the ions and core electrons with a medium basis set. A mesh cut-off energy of 10^5 Ha was employed.[56] For the relaxation of the structure, the $4 \times 4 \times 1$ Monkhorst–Pack's scheme were applied to sample the Brillouin zone. High accuracy in the electronic structure calculations was derived from using a $7 \times 7 \times 1$ *k*-point grid. The investigated system was fully optimized until the maximum force was lower than 0.05 eV $Å^{-1}$ on each atom site using the limited-memory Broyden–Fletcher–Goldfarb–Shanno scheme. For the self-consistent calculations, we utilized a criterion of a total energy convergence of 10^{-6} Ha difference. The electronic and optical properties were computed employing the more accurate Heyd–Scuseria–Ernzerhof hybrid functional (HSE06).[57–59]

3. Results and discussion

XRD was employed on the control and Mo-doped La_2O_3 in the 2θ range of 20–70° to examine the crystal structure, phase purity, and size of the crystallites (Fig. 4(a)). The diffracted peaks observed at $2\theta = 39.48°$ (012), 48.49° (111), 55.39° (112) were attributed to hexagonal (h-La_2O_3), (JCPDS no: 73-2141), and 27.02° (222) to the cubic phase (c-La_2O_3), (JCPDS no: 65-3185) of La_2O_3, while the peak broadening was related to the formation of smaller particles in the nanosize range.[60] The additional peak at 64.02°, denoted by ♠, was ascribed to

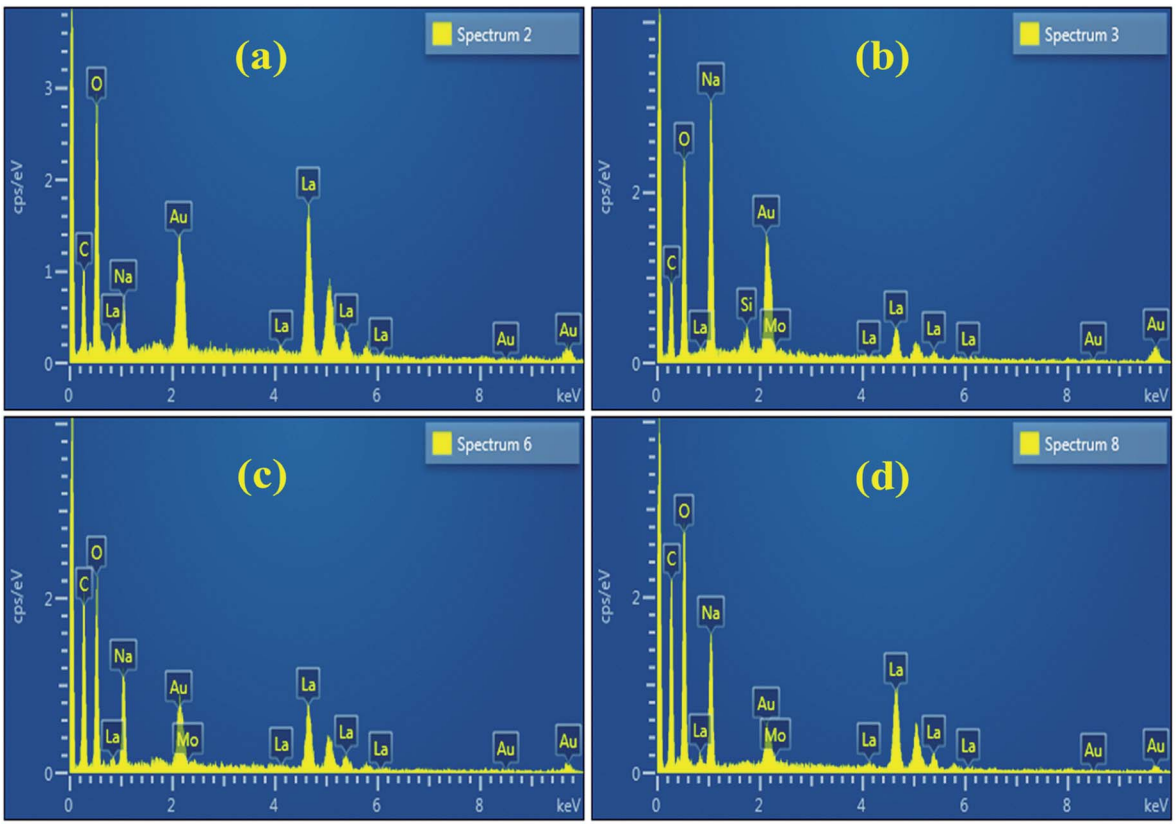

Fig. 6 (a–d) SEM-EDS analysis of La_2O_3 and Mo-doped La_2O_3.

$La(OH)_3$ (JCPDS no: 36-1481), which arose as La_2O_3 is hygroscopic in nature and upon exposure to a moist environment it quickly changes to $La(OH)_3$, as reported by Fleming *et al.*[61–63] No undesired peak appeared in the synthesized samples, suggesting the high purity of the nanostructures. The average size of the crystallites was found to be in the range of 13.1–10.6 nm, as estimated using Scherrer's formula. The shifting of the peaks to higher 2θ reflected that the crystallite size decreased with increasing the dopant amount, due to the smaller ionic radii of the dopant Mo^{4+}/Mo^{6+} (0.68 Å/0.62 Å).[60,64] This smaller radii will alter the local symmetry through the doping of heteroatoms.[65,66] The chemical composition and identification of the functional group of Mo-doped La_2O_3 were measured using FTIR analysis, as represented in Fig. 4(b). The spectra were observed in the frequency range of 500–4000 cm^{-1}. The peaks at 502, 644, 845, and 1077 cm^{-1} represented La–O bond stretching vibration.[33,34,67,68] The intense peak at 1339 cm^{-1} and small peak at 3610 cm^{-1} were ascribed to the bending and stretching of O–H vibrations, respectively, caused by the samples being processed in a moist environment.[69–71] SAED analysis revealed discrete rings, corresponding to various planes, *i.e.*, (222), (012), (111), and (112), of both the pure and doped samples, Fig. 4(c–e). Evidence of the well-crystallized material was related to these findings, which matched the XRD data. To determine the *d*-spacing, highly magnified images (at 5 nm scale) were deployed to reveal the lattice fringes for the identification of the crystallographic planes. The estimated *d*-spacing for La_2O_3 was ~0.185 nm, which satisfies the theoretical *d*-spacing of the (111) crystallographic plane of La_2O_3, Fig. 4(f). From Fig. 4(g and h), upon doping, the *d*-spacing of Mo–La_2O_3 was slightly decreased to ~0.182–0.180 nm. These calculated values matched the XRD results (Fig. 4(a)).

UV-Vis spectroscopy was utilized to investigate the optical properties of the prepared samples in terms of the maximum absorption of ultra-visible light, the band shift, and calculation of the band gap energy. Undoped and Mo-doped La_2O_3 showed absorption in the range of 280–310 nm (Fig. 5(a)). The maximum absorption peak found at 288 nm was presumably due to charge-transfer ($O^{2-} \rightarrow La^{3+}$) absorption, attributed to electronic transition π–π^*.[72] The band gap energy was evaluated using Tauc's equation, and the indirect E_g was determined to be 4.3 eV, which is consistent with previously published data.[69] More energy levels were created in the E_g of La_2O_3 upon the addition of Mo. With the increasing concentration of Mo dopant, only a small modification in the E_g was observed, *e.g.*, ~4.2 eV, at a higher concentration of Mo (Fig. 5(b)).[46,64] The band gap energy of the doped samples decreased as the crystallite size decreased, which might have been caused by reduced orientation realignment and poor crystallinity of the resulting materials.[73]

The PL spectra of the samples were investigated to determine the changes in the charge-transfer efficiency and recombination rate. The PL spectra of La_2O_3 and Mo–La_2O_3 shown in Fig. 5(c) were measured from 400 to 600 nm with a 350 nm excitation wavelength. There was a single emission peak in the spectra at 414 nm, attributed to deep levels/trap state emission in the E_g of La_2O_3. This emission transition was attributed to oxygen vacancies, singly ionized, in La_2O_3 and it occurs when a photogenerated h^+ combines with an e^- occupying an oxygen vacancy.[74–76] Due to the absence of electrons in the 4f shell of La^{3+}, it is unable to emit light from the inner atomic 4f shell when crystalline La_2O_3 is formed.[69,76,77] Near band edge (NBE) emission/transitions between MO-generated defects and the O 2p band induce violet emission between 400 and 430 nm.[78,79] Doping with Mo can suppress the recombination rate of excitons, which causes a drop in the emission peak intensity. The graph demonstrates that for a concentration of 2% Mo, the emission intensity was optimal. After this, the peak intensity decreased with the higher concentration of Mo. The higher concentrations reduce the inter-nuclear separation below a critical distance, and the excitation energy tends to move to energy-killing sites.[80–83]

The EDS spectra of the undoped sample, shown in Fig. 6(a), confirmed the existence of La and O, as well as C, which most likely originated from the carbon tape used to mount the samples. The spectra of the doped sample, Fig. 6(b–d), are nearly identical to the undoped one except for the peak of Mo ascribed to the dopant.[84] The Na peak could be attributed to the

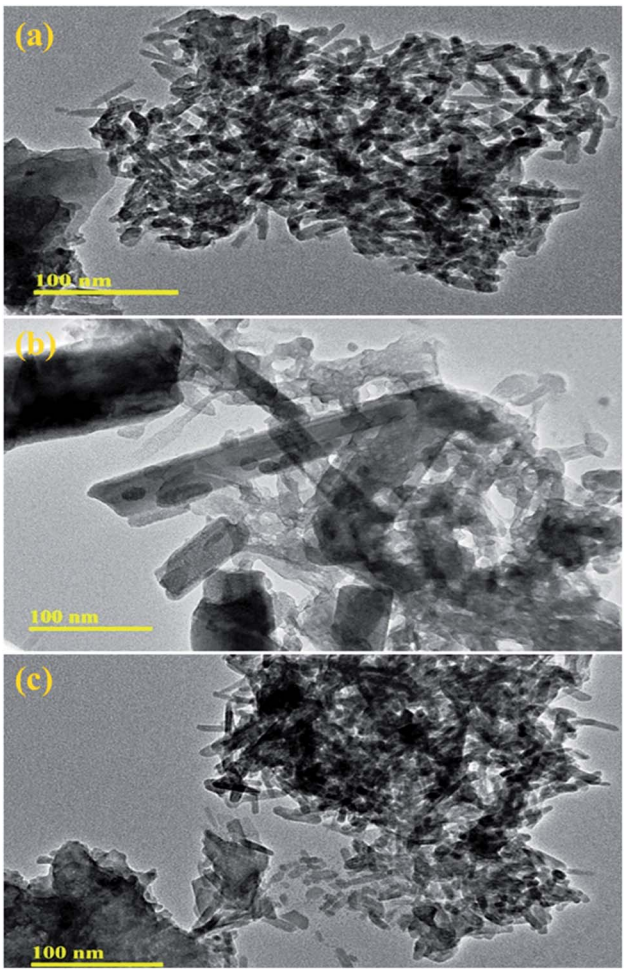

Fig. 7 HR-TEM images of (a–c) pristine and Mo (4% and 6%)-doped La_2O_3.

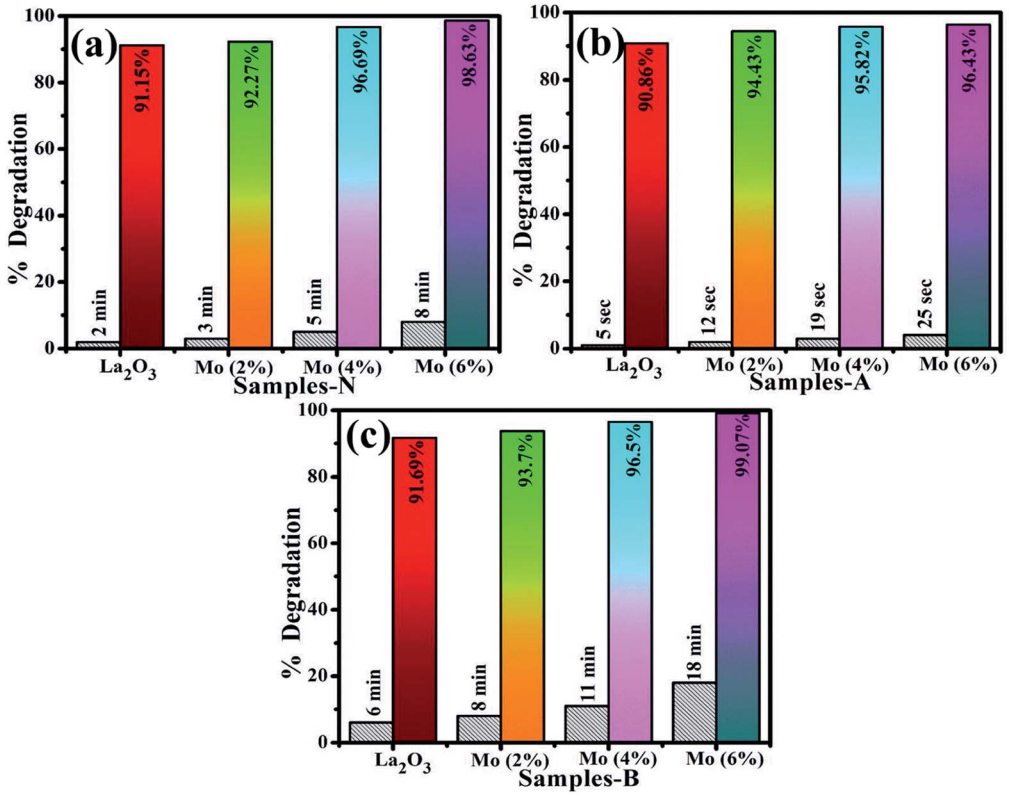

Fig. 8 Catalysis of La_2O_3, Mo–La_2O_3 (2%, 4%, and 6%) in (a) neutral, (b) acidic, and (c) basic media.

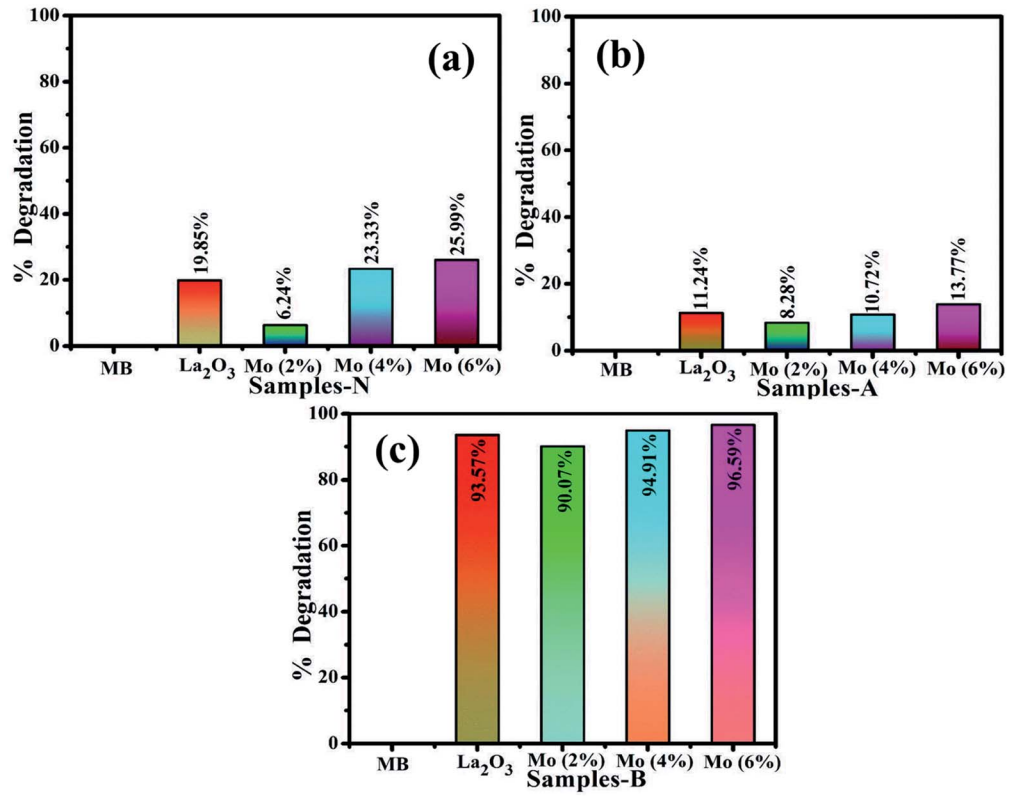

Fig. 9 Photocatalysis of La_2O_3, Mo–La_2O_3 (2%, 4%, and 6%) in (a) neutral, (b) acidic, and (c) basic media.

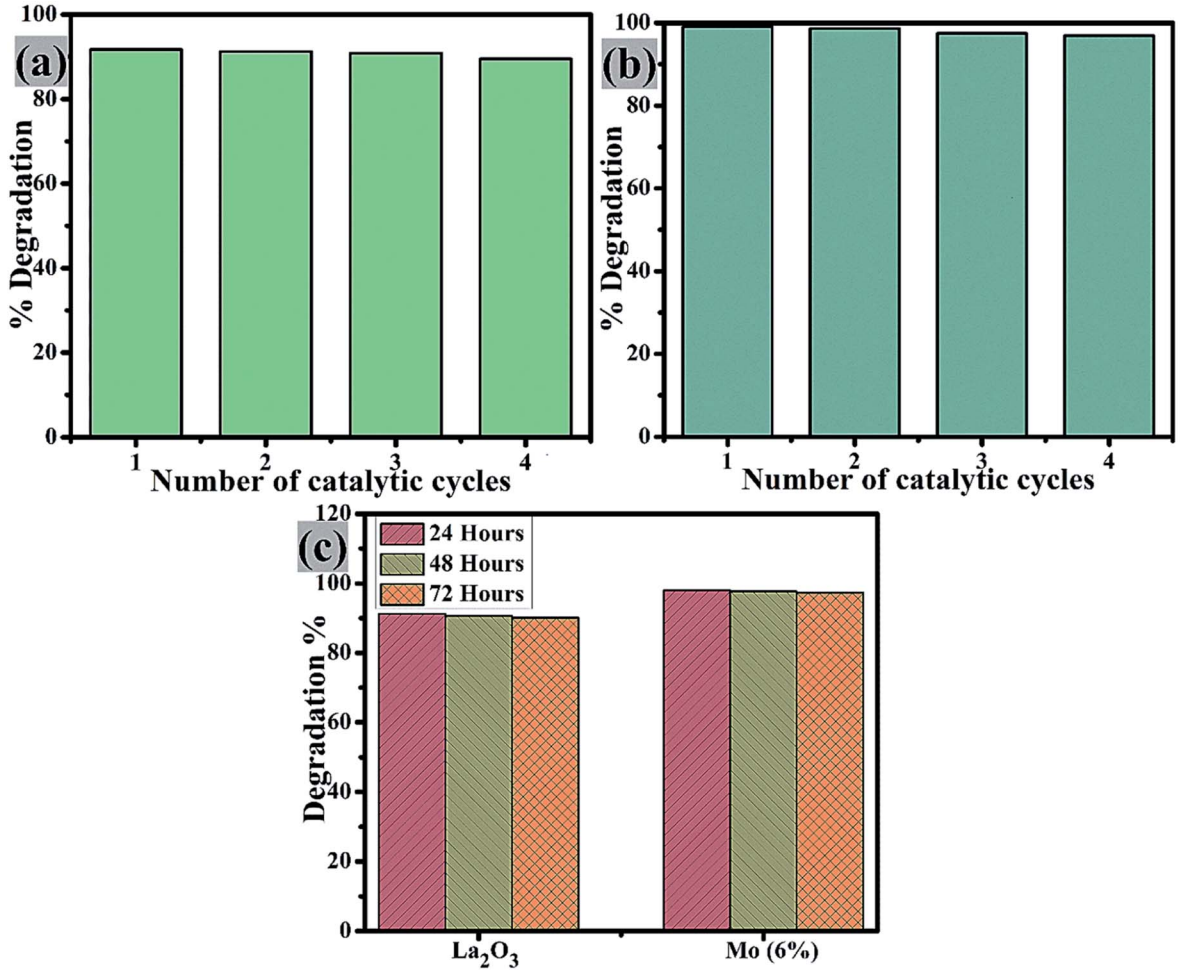

Fig. 10 Reusability of (a) La_2O_3 and (b) Mo (6%), and (c) stability comparison of the pure sample and Mo (6%).

use of NaOH to control the pH during the nanostructures synthesis.[85]

The morphology and microstructure of pure and Mo (4% and 6%)-doped La_2O_3 were further characterized by TEM. Fig. 7(a) reveals the rod-like morphology of the undoped La_2O_3 prepared by the co-precipitation method, most likely formed because of the self-assembly of molecules due to the elevated pH and removal of water.[86,87] The pristine sample showed a uniform rod-like network, Fig. 7(a). In Fig. 7(b), it appears that Mo played a role in the process of nucleation, while few undissolved Mo particles can be seen, along with the agglomeration of the rods. The rods network seemed to overlap when the concentration of Mo increased, Fig. 7(c). Agglomeration occurs at the nanoscale due to the strong attractive forces between particles.[88] Brownian agglomeration occurred here,[89] where particles stuck together loosely with an overlap of nanorods, resulting in the formation of a network, which facilitates charge transportation, leading to increased catalytic activity.

Table 1 Antimicrobial activity of pure and Mo-doped La_2O_3 nanostructures

	Inhibition zone[a] (mm)		Inhibition zone[b] (mm)	
Sample	500 μg/50 μL	1000 μg/50 μL	500 μg/50 μL	1000 μg/50 μL
La_2O_3	0	0	0.95	1.40
2% Mo–La_2O_3	0	3.35	1.05	2.15
4% Mo–La_2O_3	0	4.15	1.65	2.55
6% Mo–La_2O_3	3.15	5.05	4.65	5.45
Ciprofloxacin	4.35	4.35	5.35	5.35
DIW	0	0	0	0

[a] Inhibition area (mm) of Mo-doped La_2O_3 *S. aureus*. [b] Inhibition zone determination of Mo-doped La_2O_3 for *E. coli*.

MB was utilized to test the catalytic application of nanocatalyst in the presence of a reducing agent ($NaBH_4$). By measuring the decrease in absorbance with a UV-Vis spectrophotometer, the reactions were monitored. The pure and doped nanostructures illustrated a maximum degradation of 91.15–98.63% in neutral medium (pH 7), 90.86–96.43% in acidic medium (pH 4), and 91.69–99.07% in basic medium (pH 12), as shown in Fig. 8(a–c), respectively. In the presence of a doped nanocatalyst, reduction was enhanced. The maximum catalytic activity was achieved with Mo (6%) in all media. The crystallinity, shape, and surface area of the nanomaterials all influence

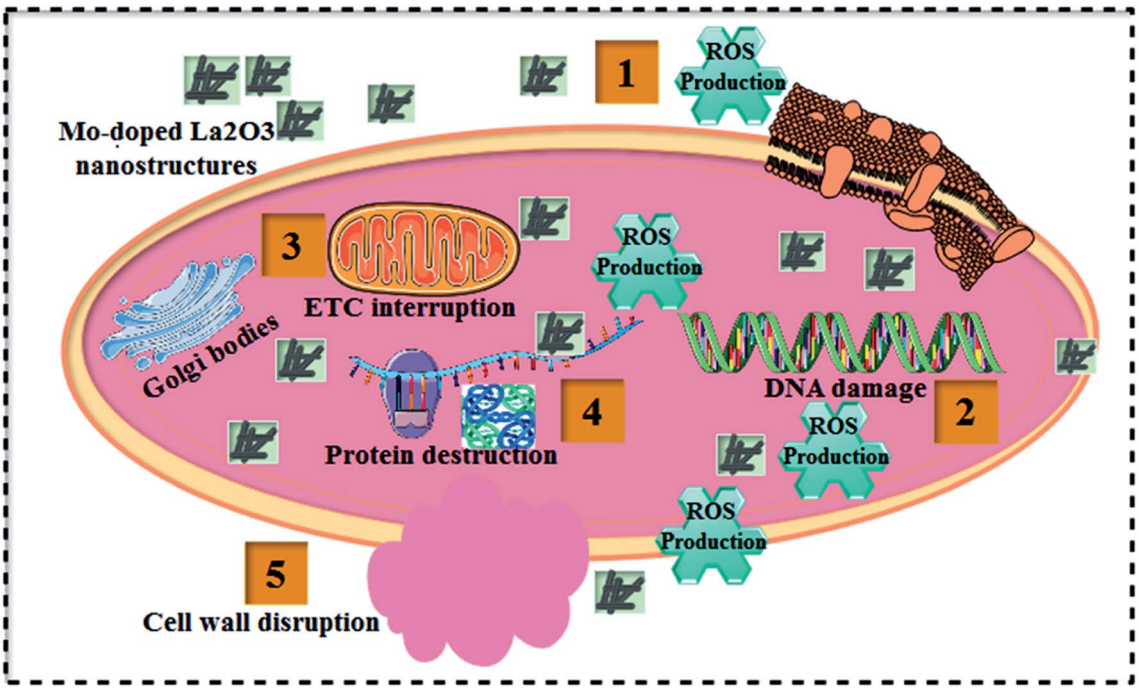

Fig. 11 Schematic illustration of the antibacterial mechanism of the prepared Mo-doped La_2O_3 nanostructures.

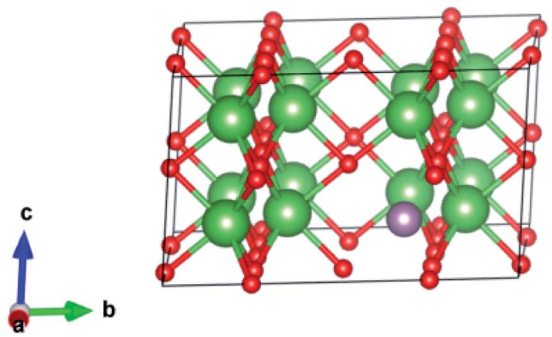

Fig. 12 Crystal structure (based on a 2 × 2 × 2 supercell) of Mo-doped La_2O_3. La is shown in green, Mo in purple, and O in red.

the catalytic activity.[90,91] During catalysis, the synthesized material serves as electron relays, reducing MB in the presence of $NaBH_4$, allowing electrons to flow from BH_4^- ions (donor) to MB (acceptor), resulting in dye reduction. Nanostructures with abundant active sites increase BH_4^- ion and dye molecule adsorption, which encourages them to react with each other.[92,93] In general, a catalyst with a wide surface area has a high catalytic efficiency since it provides more active sites.[94,95]

The photocatalysis of MB aqueous solution was investigated on undoped and doped La_2O_3 nanostructures, Fig. 9(a–c). Highly competitive degradation of 96.5% was noted for the basic medium (pH 12), within 30 min, whereas, 25.9% degradation was achieved in neutral medium (pH 7) in 60 min, and for the acidic medium (pH 4), the degradation was 21.8% in 15 min for 6% Mo-doped La_2O_3, which showed the lowest intensity of PL in Fig. 5(c), indicating a lower recombination rate. The photocatalytic response is governed by the pH of the solution, which might affect dye adsorption on the photocatalyst surface. MB is a cationic dye and its degradation was modest at low pH. However, with the rise in pH, the maximum degradation was observed. Positively charged catalyst surfaces tend to oppose the adsorption of cationic adsorbates species in an acidic medium. In basic dye solutions, surface charges tend to become negative due to the enhanced electrostatic interaction between the positively charged dye and negatively charged catalyst. As a result, dye adsorption increases, which is consistent with earlier findings.[96–98] The sample with 2% Mo doping had the lowest degradation of MB and showed the highest PL intensity. A higher recombination rate may be the cause of the lower degradation efficiency of this sample. The particle size, morphology, and surface area of nanocatalysts have a significant impact on the degradation performance. Particles with a large surface area offer more active sites for atoms, resulting in an increase in the number of redox reactions and MB reduction. Photogenerated es^- and hs^+ interact with O_2 and H_2O molecules in the solution to form highly reactive O_2^-, OH^-, and H^+ radical species, respectively. Excess H^+ and es^- interact with dye molecules, leading to MB reduction.[99,100] It is evident that degradation increases with an increasing concentration of the dopant.[74,79]

Catalyst reusability is crucial as it allows for the treatment of industrial wastewater and effluent for the highest number of cycles possible. The reusability of the control and Mo (6%) nanostructures was examined by extracting the used catalyst material. This was washed, dried, and used again for degradation in up to 4 cycles, Fig. 10(a and b). On each cycle, the efficiency of the reused catalyst showed only a slight change. It is

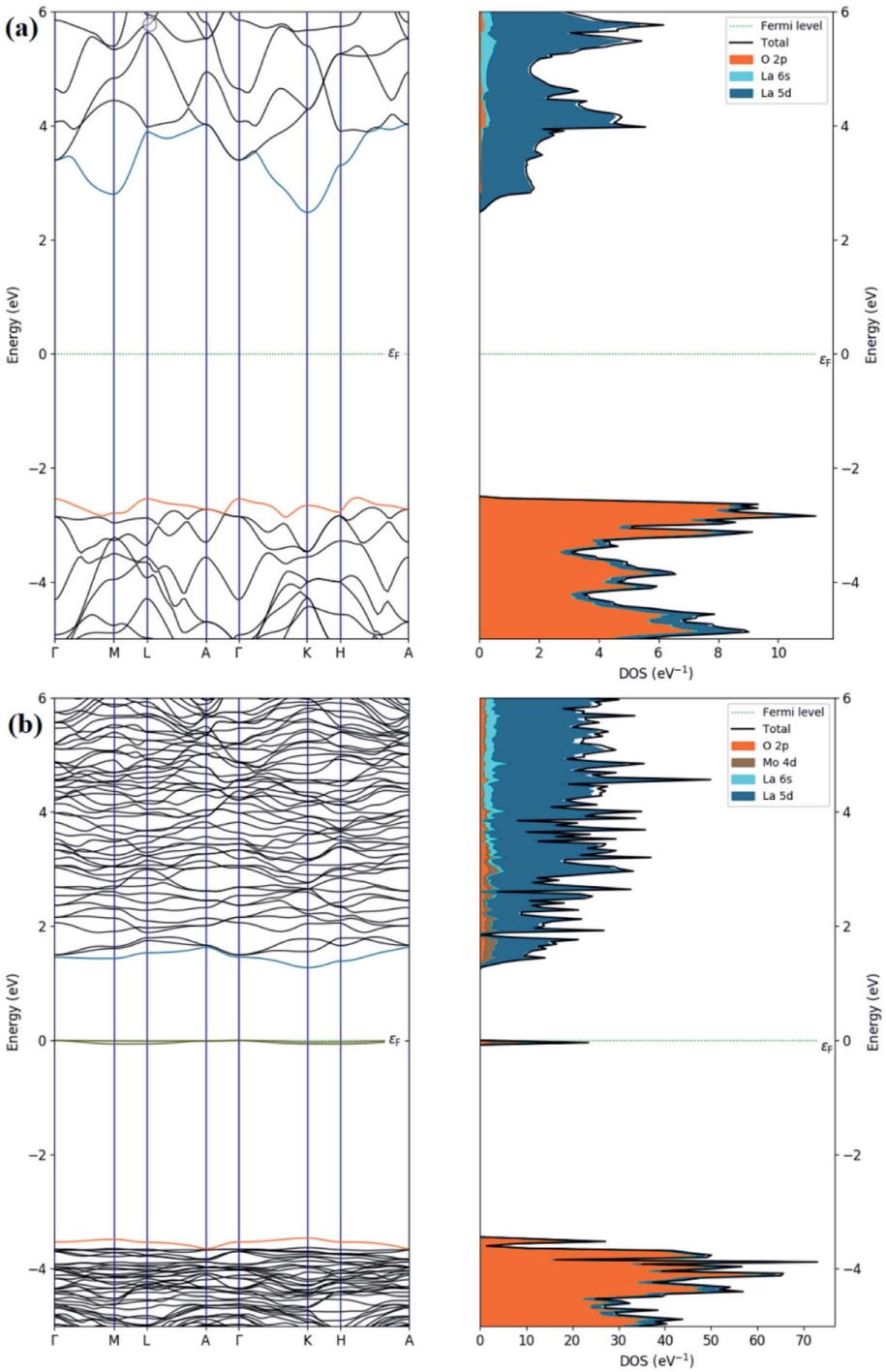

Fig. 13 Calculated band structures and total and partial DOS of (a) pristine and (b) Mo-doped La_2O_3.

worth noting that after four cycles, the degradation efficiency was only lowered by a small proportion (2%), demonstrating that the prepared nanostructures were highly stable. Furthermore, the stability of these two samples was tested by storing the degraded solution in the dark for 72 h to see if the dye degradation was stable. Dye degradation was monitored spectrophotometrically every 24 h, as illustrated in Fig. 10(c). The percentage degradation was calculated using eqn (1) and is given as the extracted results.

Table 1 shows the bactericidal efficacy of Mo-doped La_2O_3 for *S. aureus* and *E. coli*, as determined by the well diffusion technique. At minimal and maximal doses, substantial ($p < 0.05$) inhibition areas for *E. coli* were found (0.95–4.65 mm) and (1.40–5.45 mm), respectively, and (0–5.05 mm) for *S. aureus* at high dose. Except for 6% Mo–La_2O_3, none of the concentrations had any antibacterial effect against *S. aureus* at low dose. The inhibition zones for *S. aureus* and *E. coli* were compared using a negative control DI water (0 mm) and positive control

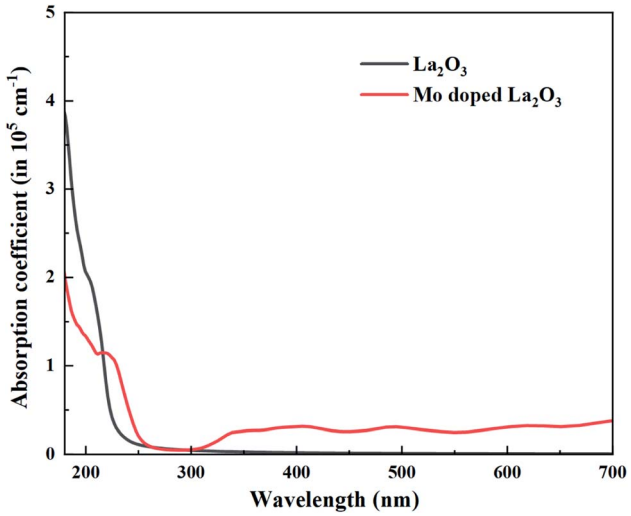

Fig. 14 Calculated absorption coefficient spectra of doping free and Mo-doped La_2O_3.

ciprofloxacin (4.35 mm) and (5.35 mm), respectively. In fact, the antibacterial activity of the nanostructures can be attributed to a variety of phenomena, including electrostatic contact or interactions with OH^- and H_2O present at the surface, both of which result in the production of reactive oxygen species (ROS), see the schematic illustration in Fig. 11. These interactions are similar to those seen in photocatalysis. Indeed, the most effective nanostructure, with 6% Mo dopant, for the degradation of MB also exhibited the best bactericidal action. In conclusion, the shape and coarseness of various nanostructures have a significant impact on the antibacterial performance.[101] MB degradation through a nanocatalyst is also influenced by the same factors.

3.1 DFT calculations

We started by performing a structural analysis of defect-free La_2O_3 prior to investigating the defects. The La_2O_3 crystallized in the hexagonal structure (space group $P\bar{3}m1$), as shown in Fig. 12. The optimized lattice parameters, $a = 3.914$ Å, $c = 6.096$ Å, showed a fair agreement with the experimentally reported values ($a = 3.939$ Å, $c = 6.136$ Å)[102] and previous theoretical studies.[103,104] To investigate Mo doping into La_2O_3 at the La site, we built a $2 \times 2 \times 2$ supercell (containing 40 atoms) and generated dopants concentration of 6.25% by replacing one La atom with one Mo atom, as illustrated in Fig. 12. The substitution of Mo impurity into the La_2O_3 lattice at the La site showed that the *a*- and *c*-lattice parameters ($a = 3.902$ Å, $c = 6.063$ Å) were little changed compared to those of the pristine sample. This difference occurs from the hexagonal lattice distortion after the Ag doping. The relaxed La–O average bond length of the pure sample was 2.645 Å, which was rather close to the experimental measurements[102] and theoretical values.[103,104] For Mo doping, the process increased the La–O (2.706 Å) bond distance because of the distortion of the crystalline structure.

Regarding the electronic properties of La_2O_3, the band structures and the density of states (DOS) were analyzed, as shown in Fig. 13. The band structure suggested a semiconducting nature with an indirect band gap (from Gamma to *K* points in the first Brillouin) of the magnitude of 4.99 eV using the HSE06 functional, which is consistent with our experimental band gap value of 4.3 eV and previous experimental data (5.34, 4.35 eV).[69,102] Comparison with the literature indicates that our HSE06 computed band gap value for La_2O_3 is in excellent agreement with that of 5.1 and 4.95 eV formerly reported using the HSE06 and G_0W_0 methods,[103,104] respectively. The valence band edge states were found to be dominated by O atoms (2p orbitals), while the unoccupied conduction band minimum states were mainly contributed by the La atom (5d orbitals). We therefore performed the electronic calculations on one doped Mo atom in the La_2O_3 by investigating the band structure and DOS, as shown in Fig. 13. As for the substitutional Mo to the La-doped La_2O_3, the band structure showed that flat bands were formed around the Fermi level, which can be beneficial, as they may act as trapping centers. We present the calculated density of electronic states for Mo-doped La_2O_3 in Fig. 13. It was found that Mo doping induced the trap gap state around the Fermi level. From the LDOS plots, the latter state was mainly constructed by Mo 3d orbitals, with a small contribution of O 2p orbitals, indicating the occurrence of the O 2p–Mo 3d hybridization. A more interesting point to notice here is the change in the band gap of the La_2O_3 supercell. However, with Mo doping, the band gap decreased to the value of 4.71 eV, which can be attributed to the variation in the bond length of La–O and the emergence of a new Mo–O bond with Mo introduction. Thus, this result is well aligned with the experimental data. Moreover, with a single La atom substitution with Mo, an in-gap state around the Fermi level was created driving a significant shift down to the VB and CB edges. To explore the absorption characteristics in the pristine and Mo-doped La_2O_3 systems, we calculated the absorption coefficient spectra *versus* the incident light wavelength using the HSE06 functional, as shown in Fig. 14. The absorption coefficients analysis showed that the pristine La_2O_3 could only absorb in the ultraviolet-light range without any absorption response in the visible-light region. The Mo doping induced a slight red-shift of the absorption edge because of the impurity in-the-gap state.

To prove the favorable adsorption of molecules on the considered materials, the adsorption energy was computed by selecting $NaBH_4$ as molecules to be absorbed on the surface of pristine and Mo-doped La_2O_3 (001) according to ref. 105 and 106:

$$E_{ads} = E_{molecule+La_2O_3(001)} - E_{La_2O_3(001)} - E_{molecule} \quad (9)$$

where $E_{molecule+La_2O_3(001)}$, $E_{La_2O_3(001)}$, and $E_{molecule}$ denote the total energies of the $NaBH_4$–La_2O_3(001) system, pure surface, and the isolated molecule, respectively. The La_2O_3 (001) and Mo-doped La_2O_3(001) surfaces were simulated using the adopted slab geometry with a (2×2) surface unit cell, separated by a vacuum distance of 15 Å,[107] as shown in Fig. 15, and a corresponding $4 \times 4 \times 1$ *k*-point mesh was employed for all these configurations. The findings revealed that the adsorption

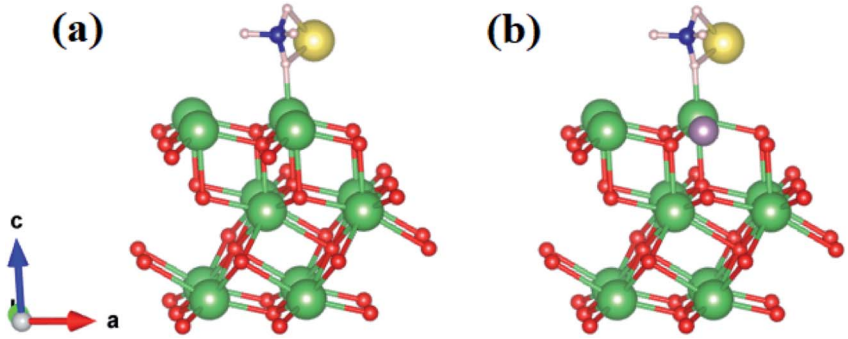

Fig. 15 Side view of the adsorption of $NaBH_4$ molecules on the (a) $La_2O_3(001)$ and (b) Mo-doped $La_2O_3(001)$ surfaces. La, O, Mo, B, H, and Na atoms are represented by green, red, purple, blue, gray and yellow balls, respectively.

energies were −4.95 and −3.25 eV in the $La_2O_3(001)$ and Mo-doped $La_2O_3(001)$ surfaces adsorbed to $NaBH_4$.

4. Conclusion

A cost-effective, co-precipitation technique was used to successfully synthesize Mo-doped La_2O_3 nanostructures. The XRD spectra confirmed the presence of hexagonal Mo along with the slight occurrence of a cubic phase in the prepared samples. The crystallite size was found to diminish from 13.1 to 10.6 nm upon doping with Mo. Combined density functional theory and experimental study supported a decrease in the E_g with an increasing amount of Mo dopant. The calculations suggest that Mo doping induces a slight red-shift in the absorption edge due to the impurity in-the-gap state. TEM revealed the rod-like morphology of La_2O_3 synthesized using the co-precipitation approach. The EDS spectra demonstrated the elemental composition and successful Mo doping. When compared to undoped samples, Mo-doped La_2O_3 nanostructures demonstrated better catalytic potential of up to 99%. Furthermore, the synthesized nanostructures exhibited substantial bactericidal efficacy against *S. aureus* and *E. coli* bacteria.

Conflicts of interest

There are no conflicts to declare.

Acknowledgements

We are immensely thankful to HEC Pakistan (SRGP# 21-1669) and the Core Research Facilities, KFUPM (Dhahran, Saudi Arabia) for their assistance. S. Goumri-Said thanks the Alfaisal University Research Office in Saudi Arabia for financing this research project C20431.

References

1 R. Rajkumar, G. Ezhumalai and M. Gnanadesigan, A green approach for the synthesis of silver nanoparticles by Chlorella vulgaris and its application in photocatalytic dye degradation activity, *Environ. Technol. Innovation*, 2021, **21**, 101282.

2 M. M. Hasan, M. A. Shenashen, M. N. Hasan, H. Znad, M. S. Salman and M. R. Awual, Natural biodegradable polymeric bioadsorbents for efficient cationic dye encapsulation from wastewater, *J. Mol. Liq.*, 2021, **323**, 114587.

3 A. Raza, M. Ikram, M. Aqeel, M. Imran, A. Ul-Hamid, K. N. Riaz and S. Ali, Enhanced industrial dye degradation using Co doped in chemically exfoliated MoS_2 nanosheets, *Appl. Nanosci.*, 2020, **10**(5), 1535–1544.

4 M. M. Ghangrekar and P. Chatterjee, Water Pollutants Classification and Its Effects on Environment, in *Carbon Nanotubes for Clean Water. Carbon Nanostructures*, ed. R. Das, Springer, 2018 Aug 13, pp. 11–26.

5 R. N. Bharagava, G. Saxena and S. I. Mulla, Introduction to industrial wastes containing organic and inorganic pollutants and bioremediation approaches for environmental management, in *Bioremediation of Industrial Waste for Environmental Safety*, Springer Nature, 2020 June 30, pp. 1–18.

6 N. Sivarajasekar and R. Baskar, Adsorption of basic red 9 on activated waste Gossypium hirsutum seeds: process modeling, analysis and optimization using statistical design, *J. Ind. Eng. Chem.*, 2014, **20**(5), 2699–2709.

7 M. Rafatullah, O. Sulaiman, R. Hashim and A. Ahmad, Adsorption of methylene blue on low-cost adsorbents: a review, *J. Hazard. Mater.*, 2010, **177**(1–3), 70–80.

8 Y. Hua, J. Xiao, Q. Zhang, C. Cui and C. Wang, Facile synthesis of surface-functionalized magnetic nanocomposites for effectively selective adsorption of cationic dyes, *Nanoscale Res. Lett.*, 2018, **13**(1), 1–9.

9 H. Demissie, G. An, R. Jiao, T. Ritigala, S. Lu and D. Wang, Modification of high content nanocluster-based coagulation for rapid removal of dye from water and the mechanism, *Sep. Purif. Technol.*, 2021, **259**, 117845.

10 Q. Feng, B. Gao, Q. Yue and K. Guo, Flocculation performance of papermaking sludge-based flocculants in different dye wastewater treatment: comparison with commercial lignin and coagulants, *Chemosphere*, 2021, **262**, 128416.

11 J. Fito, N. Tefera and S. W. Van Hulle, An integrated treatment technology for blended wastewater of the sugar

industry and ethanol distillery, *Environ. Processes*, 2019, **6**(2), 475–491.

12 S. Ye, M. Yan, X. Tan, J. Liang, G. Zeng, H. Wu, B. Song, C. Zhou, Y. Yang and H. Wang, Facile assembled biochar-based nanocomposite with improved graphitization for efficient photocatalytic activity driven by visible light, *Appl. Catal., B*, 2019, **250**, 78–88.

13 S. Ye, W. Xiong, J. Liang, H. Yang, H. Wu, C. Zhou, L. Du, J. Guo, W. Wang, L. Xiang and G. Zeng, Refined regulation and nitrogen doping of biochar derived from ramie fiber by deep eutectic solvents (DESs) for catalytic persulfate activation toward non-radical organics degradation and disinfection, *J. Colloid Interface Sci.*, 2021, **601**, 544–555.

14 J. Hassan, M. Ikram, A. Ul-Hamid, M. Imran, M. Aqeel and S. J. Ali, Application of chemically exfoliated boron nitride nanosheets doped with co to remove organic pollutants rapidly from textile water, *Nanoscale Res. Lett.*, 2020, **15**(1), 1–3.

15 F. H. Dodd, Mastitis—progress on control, *J. Dairy Sci.*, 1983, **66**(8), 1773–1780.

16 A. Haider, M. Ijaz, S. Ali, J. Haider, M. Imran, H. Majeed, I. Shahzadi, M. M. Ali, J. A. Khan and M. Ikram, Green synthesized phytochemically (Zingiber officinale and Allium sativum) reduced nickel oxide nanoparticles confirmed bactericidal and catalytic potential, *Nanoscale Res. Lett.*, 2020, **15**(1), 1.

17 M. Ali, M. Ikram, M. Ijaz, A. Ul-Hamid, M. Avais and A. A. Anjum, Green synthesis and evaluation of n-type ZnO nanoparticles doped with plant extract for use as alternative antibacterials, *Appl. Nanosci.*, 2020, **10**, 3787–3803.

18 P. M. Hawkey, The growing burden of antimicrobial resistance, *J. Antimicrob. Chemother.*, 2008, **62**(suppl_1), i1–i9.

19 O. O. Komolafe, Antibiotic resistance in bacteria-an emerging public health problem, *Malawi Med. J.*, 2003, **15**(2), 63–67.

20 Z. Cai, Y. Sun, W. Liu, F. Pan, P. Sun and J. Fu, An overview of nanomaterials applied for removing dyes from wastewater, *Environ. Sci. Pollut. Res.*, 2017, **24**(19), 15882–15904.

21 A. Haider, M. Ijaz, M. Imran, M. Naz, H. Majeed, J. A. Khan, M. M. Ali and M. Ikram, Enhanced bactericidal action and dye degradation of spicy roots' extract-incorporated fine-tuned metal oxide nanoparticles, *Appl. Nanosci.*, 2020, **10**(4), 1095–1104.

22 N. Savage and M. S. Diallo, Nanomaterials and water purification: opportunities and challenges, *J. Nanopart. Res.*, 2005, **7**(4), 331–342.

23 C. Siriwong, N. Wetchakun, B. Inceesungvorn, D. Channei, T. Samerjai and S. Phanichphant, Doped-metal oxide nanoparticles for use as photocatalysts, *Prog. Cryst. Growth Charact. Mater.*, 2012, **58**(2–3), 145–163.

24 V. Vamathevan, R. Amal, D. Beydoun, G. Low and S. McEvoy, Photocatalytic oxidation of organics in water using pure and silver-modified titanium dioxide particles, *J. Photochem. Photobiol., A*, 2002, **148**(1–3), 233–245.

25 V. Kumari, N. Kumar, S. Yadav, A. Mittal and S. Sharma, Novel mixed metal oxide (ZnO, La_2O_3, CeO_2) synthesized via hydrothermal and solution combustion process–a comparative study and their photocatalytic properties, *Mater. Today: Proc.*, 2019, **19**, 650–657.

26 J. Lu, I. Batjikh, J. Hurh, Y. Han, H. Ali, R. Mathiyalagan, C. Ling, J. C. Ahn and D. C. Yang, Photocatalytic degradation of methylene blue using biosynthesized zinc oxide nanoparticles from bark extract of Kalopanax septemlobus, *Optik*, 2019, **182**, 980–985.

27 M. Mittal, A. Gupta and O. P. Pandey, Role of oxygen vacancies in Ag/Au doped CeO_2 nanoparticles for fast photocatalysis, *Sol. Energy*, 2018, **165**, 206–216.

28 Y. Huo, X. Zhang, Y. Jin, J. Zhu and H. Li, Highly active $La_2O_3/Ti_{1-x}B_xO_2$ visible light photocatalysts prepared under supercritical conditions, *Appl. Catal., B*, 2008, **83**(1–2), 78–84.

29 N. R. Radwan, Effects of La_2O_3-doping on physicochemical surface and catalytic properties of nickel and manganese oxides supported on alumina, *Appl. Catal., A*, 2004, **257**(2), 177–191.

30 R. A. Ismail, F. A. Fadhil and H. H. Rashed, Novel route to prepare lanthanum oxide nanoparticles for optoelectronic devices, *Int. J. Mod. Phys. B*, 2020, **34**(13), 2050134.

31 K. Mustofa, Y. Yulizar, A. Saefumillah and D. O. Apriandanu, La_2O_3 nanoparticles formation using Nothopanax scutellarium leaf extract in two-phase system and photocatalytic activity under UV light irradiation, *IOP Conf. Ser.: Mater. Sci. Eng.*, 2020, **902**(1), 012018.

32 M. Salavati-Niasari, G. Hosseinzadeh and F. Davar, Synthesis of lanthanum hydroxide and lanthanum oxide nanoparticles by sonochemical method, *J. Alloys Compd.*, 2011, **509**(10), 4098–4103.

33 M. Veerasingam, B. Murugesan and S. Mahalingam, Ionic liquid mediated morphologically improved lanthanum oxide nanoparticles by Andrographis paniculata leaves extract and its biomedical applications, *J. Rare Earths*, 2020, **38**(3), 281–291.

34 G. Ravi, M. Sarasija, D. Ayodhya, L. S. Kumari and D. Ashok, Facile synthesis, characterization and enhanced catalytic reduction of 4-nitrophenol using $NaBH_4$ by undoped and Sm^{3+}, Gd^{3+}, Hf^{3+} doped La_2O_3 nanoparticles, *Nano Convergence*, 2019, **6**(1), 1–9.

35 F. J. Jing, L. Wang, Y. W. Liu, R. K. Fu, X. B. Zhao, R. Shen, N. Huang and P. K. Chu, Hemocompatibility of lanthanum oxide films fabricated by dual plasma deposition, *Thin Solid Films*, 2006, **515**(3), 1219–1222.

36 R. Bomila, S. Srinivasan, S. Gunasekaran and A. Manikandan, Enhanced photocatalytic degradation of methylene blue dye, opto-magnetic and antibacterial behaviour of pure and La-doped ZnO nanoparticles, *J. Supercond. Novel Magn.*, 2018, **31**(3), 855–864.

37 S. Zhong, B. Deng, A. Xu and S. Wang, Preparation and Characterization of 3D Flower-like La_2O_3 Nanostructures, *Curr. Nanosci.*, 2011, **7**(3), 407–414.

38 A. Neumann and D. Walter, The thermal transformation from lanthanum hydroxide to lanthanum hydroxide oxide, *Thermochim. Acta*, 2006, **445**(2), 200–204.
39 S. J. Kim, W. K. Han, S. G. Kang, M. S. Han and Y. H. Cheong, Formation of lanthanum hydroxide and oxide via precipitation, *Solid State Phenom.*, 2008, **135**, 23–26.
40 S. J. Nejad, H. Abolghasemi, M. A. Moosavian, A. Golzary and M. G. Maragheh, Fractional factorial design for the optimization of hydrothermal synthesis of lanthanum oxide nanoparticles under supercritical water condition, *J. Supercrit. Fluids*, 2010, **52**(3), 292–297.
41 X. Wang, M. Wang, H. Song and B. Ding, A simple sol–gel technique for preparing lanthanum oxide nanopowders, *Mater. Lett.*, 2006, **60**(17–18), 2261–2265.
42 N. Zhang, R. Yi, L. Zhou, G. Gao, R. Shi, G. Qiu and X. Liu, Lanthanide hydroxide nanorods and their thermal decomposition to lanthanide oxide nanorods, *Mater. Chem. Phys.*, 2009, **114**(1), 160–167.
43 P. G. Krishna and N. J. Tharayil, Dielectric properties of lanthanum oxide nanoparticle synthesized using chemical co-precipitation method, *Am. Inst. Phys., Conf. Ser.*, 2019, **2162**, 020079.
44 Q. L. Zhang, Z. J. Ji, J. Zhou, X. C. Zhao and X. Z. Lan, Preparation of lanthanum oxide nanoparticles by chemical precipitation method, *Mater. Sci. Forum*, 2012, **724**, 233–236.
45 L. Wang, Y. Ma, Y. Wang, S. Liu and Y. Deng, Efficient synthesis of glycerol carbonate from glycerol and urea with lanthanum oxide as a solid base catalyst, *Catal. Commun.*, 2011, **12**(15), 1458–1462.
46 F. Bozheyev, E. M. Akinoglu, L. Wu, S. Lou and M. Giersig, Effect of Mo-doping in SnO_2 thin film photoanodes for water oxidation, *Int. J. Hydrogen Energy*, 2020, **45**(58), 33448–33456.
47 V. I. Merupo, S. Velumani, G. Oza, M. Makowska-Janusik and A. Kassiba, Structural, electronic and optical features of molybdenum-doped bismuth vanadium oxide, *Mater. Sci. Semicond. Process.*, 2015, **31**, 618–623.
48 Y. C. Lin, B. L. Wang, W. T. Yen and C. H. Shen, Surface textured molybdenum doped zinc oxide thin films prepared for thin film solar cells using pulsed direct current magnetron sputtering, *Thin Solid Films*, 2011, **519**(16), 5571–5576.
49 S. Zhang, F. Ding, X. Luo and X. Lin, Facile synthesis of hierarchical Mo-doped S/BiOCl heterostructured spheres and its excellent photo/thermocatalytic activity under near room temperature, *J. Alloys Compd.*, 2016, **673**, 93–101.
50 J. M. Small and H. Hintelmann, Methylene blue derivatization then LC–MS analysis for measurement of trace levels of sulfide in aquatic samples, *Anal. Bioanal. Chem.*, 2007, **387**(8), 2881–2886.
51 M. J. Muñoz-Batista and R. Luque, Heterogeneous Photocatalysis, *ChemEngineering*, 2021, **5**(2), 26.
52 J. Ananpattarachai, P. Kajitvichyanukul and S. Seraphin, Visible light absorption ability and photocatalytic oxidation activity of various interstitial N-doped TiO_2 prepared from different nitrogen dopants, *J. Hazard. Mater.*, 2009, **168**(1), 253–261.
53 A. Gnanaprakasam, V. M. Sivakumar and M. Thirumarimurugan, Influencing parameters in the photocatalytic degradation of organic effluent via nanometal oxide catalyst: a review, *Indian J. Eng. Mater. Sci.*, 2015, **2015**, 16.
54 J. P. Perdew, K. Burke and M. Ernzerhof, Generalized gradient approximation made simple, *Phys. Rev. Lett.*, 1996, **77**(18), 3865.
55 S. Smidstrup, T. Markussen, P. Vancraeyveld, J. Wellendorff, J. Schneider, T. Gunst, B. Verstichel, D. Stradi, P. A. Khomyakov, U. G. Vej-Hansen and M. E. Lee, QuantumATK: an integrated platform of electronic and atomic-scale modelling tools, *J. Phys.: Condens. Matter*, 2019, **32**(1), 015901.
56 M. J. van Setten, M. Giantomassi, E. Bousquet, M. J. Verstraete, D. R. Hamann, X. Gonze and G. M. Rignanese, The PseudoDojo: Training and grading a 85 element optimized norm-conserving pseudopotential table, *Comput. Phys. Commun.*, 2018, **226**, 39–54.
57 J. Heyd, G. E. Scuseria and M. Ernzerhof, Hybrid functionals based on a screened Coulomb potential, *J. Chem. Phys.*, 2003, **118**(18), 8207–8215.
58 M. B. Kanoun, S. Goumri-Said, U. Schwingenschlögl and A. Manchon, Magnetism in Sc-doped ZnO with zinc vacancies: a hybrid density functional and GGA + U approaches, *Chem. Phys. Lett.*, 2012, **532**, 96–99.
59 B. U. Haq, M. B. Kanoun, R. Ahmed, M. Bououdina and S. Goumri-Said, Hybrid functional calculations of potential hydrogen storage material: complex dimagnesium iron hydride, *Int. J. Hydrogen Energy*, 2014, **39**(18), 9709–9717.
60 B. P. Gangwar, S. Irusta and S. Sharma, Physicochemical and optical properties of one-pot combustion synthesized Pr doped La_2O_3/La $(OH)_3$, *J. Lumin.*, 2020, **219**, 116893.
61 J. G. Kang, Y. I. Kim, D. W. Cho and Y. Sohn, Synthesis and physicochemical properties of $La(OH)_3$ and La_2O_3 nanostructures, *Mater. Sci. Semicond. Process.*, 2015, **40**, 737–743.
62 P. Fleming, R. A. Farrell, J. D. Holmes and M. A. Morris, The rapid formation of $La(OH)_3$ from La_2O_3 powders on exposureto water vapor, *J. Am. Ceram. Soc.*, 2010, **93**(4), 1187–1194.
63 K. Kim, D. Kim, T. Kim, B. G. Kim, D. Ko, J. Lee, Y. Han, J. C. Jung and H. B. Na, Synthesis of mesoporous lanthanum hydroxide with enhanced adsorption performance for phosphate removal, *RSC Adv.*, 2019, **9**(27), 15257–15264.
64 L. G. Devi and B. N. Murthy, Characterization of Mo doped TiO_2 and its enhanced photo catalytic activity under visible light, *Catal. Lett.*, 2008, **125**(3), 320–330.
65 G. Murugadoss, J. Ma, X. Ning and M. R. Kumar, Selective metal ions doped CeO_2 nanoparticles for excellent photocatalytic activity under sun light and supercapacitor application, *Inorg. Chem. Commun.*, 2019, **109**, 107577.

66 K. Yang, J. Rong, J. Feng, Y. Zhuang, H. Zhao, L. Wang, J. Ni, S. Tao, F. Shao and C. Ding, Excellent wear resistance of plasma-sprayed amorphous Al_2O_3–$Y_3Al_5O_{12}$ ceramic coating, *Surf. Coat. Technol.*, 2017, **326**, 96–102.

67 D. Rattanaphra, P. Soodjit, A. Thanapimmetha, M. Saisriyoot and P. Srinophakun, Synthesis, characterization and catalytic activity studies of lanthanum oxide from Thai monazite ore for biodiesel production, *Renewable Energy*, 2019, **131**, 1128–1137.

68 S. Karthikeyan, M. Selvapandiyan, S. Shanavas, P. M. Anbarasan and R. Acevedo, A role of annealing temperature on the properties of lanthanum oxide (La_2O_3) microplates by reflux routes, *Mater. Today: Proc.*, 2020, **26**, 3576–3578.

69 Q. Mu and Y. Wang, Synthesis, characterization, shape-preserved transformation, and optical properties of $La(OH)_3$, $La_2O_2CO_3$, and La_2O_3 nanorods, *J. Alloys Compd.*, 2011, **509**(2), 396–401.

70 H. Zhu, D. Yang, H. Yang, L. Zhu, D. Li, D. Jin and K. Yao, Reductive hydrothermal synthesis of $La(OH)_3$: Tb^{3+} nanorods as a new green emitting phosphor, *J. Nanopart. Res.*, 2008, **10**(2), 307–312.

71 T. Levan, M. Che, J. M. Tatibouet and M. Kermarec, Infrared study of the formation and stability of $La_2O_2CO_3$ during the oxidative coupling of methane on La_2O_3, *J. Catal.*, 1993, **142**(1), 18–26.

72 K. Skrabania, A. Miasnikova, A. M. Bivigou-Koumba, D. Zehm and A. Laschewsky, Examining the UV-vis absorption of RAFT chain transfer agents and their use for polymer analysis, *Polym. Chem.*, 2011, **2**(9), 2074–2083.

73 A. M. Raba-Páez, D. J. O. Malafatti, C. A. Parra-Vargas, E. C. Paris and M. Rincón-Joya, Effect of tungsten doping on the structural, morphological and bactericidal properties of nanostructured CuO, *PLoS One*, 2020, **15**(9), e0239868.

74 C. Bilel, R. Jbeli, I. B. Jemaa, A. Boukhachem, F. Saadallah, M. Amlouk and H. Ezzaouïa, Physical investigations on annealed structure Cu/La_2O_3 for photocatalytic application under sunlight, *J. Mater. Sci.: Mater. Electron.*, 2020, 1–3.

75 R. Jbeli, A. Boukhachem, I. B. Jemaa, N. Mahdhi, F. Saadallah, H. Elhouichet, S. Alleg, M. Amlouk and H. Ezzaouïa, An enhancement of photoluminescence property of Ag doped La_2O_3 thin films at room temperature, *Spectrochim. Acta, Part A*, 2017, **184**, 71–81.

76 C. G. Hu, H. Liu, W. T. Dong, Y. Y. Zhang, G. Bao, C. S. Lao and Z. L. Wang, $La(OH)_3$ and La_2O_3 nanobelts—synthesis and physical properties, *Adv. Mater.*, 2007, **19**(3), 470–474.

77 J. Lucas, P. Lucas, T. Le Mercier, A. Rollat and W. G. Davenport, Introduction to rare earth luminescent materials, *Rare Earths*, 2015, 251–280.

78 A. Loukil, A. Boukhachem, M. B. Amor, M. Ghamnia and K. Raouadi, Effects of potassium incorporation on the structural, optical, vibrational and electrical properties of NiO sprayed thin films for p-type optical windows, *Ceram. Int.*, 2016, **42**(7), 8274–8289.

79 R. Jbeli, M. Lahmar, C. Bilel, F. Saadallah, H. I. Ouzari, M. Bouaïcha and M. Amlouk, Structural and optical investigations on sprayed Co doped La_2O_3 thin films along with photocatalytic and anti-bacterial applications, *Optik*, 2021, **242**, 166837.

80 C. Yu, K. Yang, Q. Shu, C. Y. Jimmy, F. Cao, X. Li and X. Zhou, Preparation, characterization and photocatalytic performance of Mo-doped ZnO photocatalysts, *Sci. China: Chem.*, 2012, **55**(9), 1802–1810.

81 R. S. Yadav, S. J. Dhoble and S. B. Rai, Improved photon upconversion photoluminescence and intrinsic optical bistability from a rare earth co-doped lanthanum oxide phosphor via Bi^{3+} doping, *New J. Chem.*, 2018, **42**(9), 7272–7282.

82 R. S. Yadav, R. V. Yadav, A. Bahadur and S. B. Rai, Enhanced white light emission from a Tm^{3+}/Yb^{3+}/Ho^{3+} co-doped $Na_4ZnW_3O_{12}$ nano-crystalline phosphor via Li^+ doping, *RSC Adv.*, 2016, **6**(57), 51768–51776.

83 R. S. Yadav, R. K. Verma and S. B. Rai, Intense white light emission in Tm^{3+}/Er^{3+}/Yb^{3+} co-doped Y_2O_3–ZnO nano-composite, *J. Phys. D: Appl. Phys.*, 2013, **46**(27), 275101.

84 B. M. Jaffar, H. C. Swart, H. S. Ahmed, A. Yousif and R. E. Kroon, Luminescence properties of Bi doped La_2O_3 powder phosphor, *J. Lumin.*, 2019, **209**, 217–224.

85 M. Ikram, S. Aslam, A. Haider, S. Naz, A. Ul-Hamid, A. Shahzadi, M. Ikram, J. Haider, S. O. Ahmad and A. R. Butt, Doping of Mg on ZnO Nanorods Demonstrated Improved Photocatalytic Degradation and Antimicrobial Potential with Molecular Docking Analysis, *Nanoscale Res. Lett.*, 2021, **16**(1), 1–6.

86 G. Amin, M. H. Asif, A. Zainelabdin, S. Zaman, O. Nur and M. Willander, Influence of pH, precursor concentration, growth time, and temperature on the morphology of ZnO nanostructures grown by the hydrothermal method, *J. Nanomater.*, 2011, **2011**, 269692.

87 S. R. Khan, S. Jamil, M. R. Janjua and R. A. Khera, Synthesis of ferric oxyhydroxide nanoparticles and ferric oxide nanorods by reflux assisted coprecipitation method and comparative study of their thermal properties, *Mater. Res. Express*, 2017, **4**(11), 115019.

88 F. Henry, P. Marchal, J. Bouillard, A. Vignes, O. Dufaud and L. Perrin, The effect of agglomeration on the emission of particles from nanopowders flow, in *14 International Symposium on Loss Prevention and Safety Promotion in the Process Industry*, 2013 May 12, vol. 31, pp. 811–816.

89 A. Singer, Z. Barakat, S. Mohapatra and S. S. Mohapatra, Nanoscale drug-delivery systems: in vitro and in vivo characterization, in *Nanocarriers for Drug Delivery*, Elsevier, 2019 Jan 1, pp. 395–419.

90 A. Shahpal, M. Aziz Choudhary and Z. Ahmad, An investigation on the synthesis and catalytic activities of pure and Cu-doped zinc oxide nanoparticles, *Cogent Chem.*, 2017, **3**(1), 1301241.

91 M. Rashid, M. Ikram, A. Haider, S. Naz, J. Haider, A. Ul-Hamid, A. Shahzadi and M. Aqeel, Photocatalytic, dye degradation, and bactericidal behavior of Cu-doped ZnO

nanorods and their molecular docking analysis, *Dalton Trans.*, 2020, **49**(24), 8314–8330.

92 M. Ikram, T. Inayat, A. Haider, A. Ul-Hamid, J. Haider, W. Nabgan, A. Saeed, A. Shahbaz, S. Hayat, K. Ul-Ain and A. R. Butt, Graphene oxide-doped MgO nanostructures for highly efficient dye degradation and bactericidal action, *Nanoscale Res. Lett.*, 2021, **16**(1), 1.

93 A. A. Fairuzi, N. N. Bonnia, R. M. Akhir, M. A. Abrani and H. M. Akil, Degradation of methylene blue using silver nanoparticles synthesized from imperata cylindrica aqueous extract, *IOP Conf. Ser. Earth Environ. Sci.*, 2018, **105**, 012018.

94 W. Shen, X. Dong, Y. Zhu, H. Chen and J. Shi, Mesoporous CeO_2 and CuO-loaded mesoporous CeO_2: synthesis, characterization, and CO catalytic oxidation property, *Microporous Mesoporous Mater.*, 2005, **85**(1–2), 157–162.

95 M. F. Luo, Y. P. Song, J. Q. Lu, X. Y. Wang and Z. Y. Pu, Identification of CuO Species in high surface area CuO–CeO_2 catalysts and their catalytic activities for CO oxidation, *J. Phys. Chem. C*, 2007, **111**(34), 12686–12692.

96 T. Nguyen Thi Thu, N. Nguyen Thi, V. Tran Quang, K. Nguyen Hong, T. Nguyen Minh and N. Le Thi Hoai, Synthesis, characterisation, and effect of pH on degradation of dyes of copper-doped TiO_2, *J. Exp. Nanosci.*, 2016, **11**(3), 226–238.

97 E. Haque, J. W. Jun and S. H. Jhung, Adsorptive removal of methyl orange and methylene blue from aqueous solution with a metal-organic framework material, iron terephthalate (MOF-235), *J. Hazard. Mater.*, 2011, **185**(1), 507–511.

98 K. P. Singh, D. Mohan, S. Sinha, G. S. Tondon and D. Gosh, Color removal from wastewater using low-cost activated carbon derived from agricultural waste material, *Ind. Eng. Chem. Res.*, 2003, **42**(9), 1965–1976.

99 S. V. Kite, D. J. Sathe, A. N. Kadam, S. S. Chavan and K. M. Garadkar, Highly efficient photodegradation of 4-nitrophenol over the nano-TiO_2 obtained from chemical bath deposition technique, *Res. Chem. Intermed.*, 2020, **46**(2), 1255–1282.

100 S. O. Ahmad, M. Ikram, M. Imran, S. Naz, A. Ul-Hamid, A. Haider, A. Shahzadi and J. Haider, Novel prism shaped C_3N_4-doped Fe@Co_3O_4 nanocomposites and their dye degradation and bactericidal potential with molecular docking study, *RSC Adv.*, 2021, **11**(38), 23330–23344.

101 A. Arfaoui, A. Mhamdi, N. Besrour, S. Touihri, H. I. Ouzari, Z. A. Alrowaili and M. Amlouk, Investigations into the physical properties of SnO_2/MoO_3 and SnO_2/WO_3 bi-layered structures along with photocatalytic and antibacterial applications, *Thin Solid Films*, 2018, **648**, 12–20.

102 S. I. Kimura, F. Arai and M. Ikezawa, Optical study on electronic structure of rare-earth sesquioxides, *J. Phys. Soc. Jpn.*, 2000, **69**(10), 3451–3457.

103 R. Gillen, S. J. Clark and J. Robertson, Nature of the electronic band gap in lanthanide oxides, *Phys. Rev. B: Condens. Matter Mater. Phys.*, 2013, **87**(12), 125116.

104 H. Jiang, P. Rinke and M. Scheffler, Electronic properties of lanthanide oxides from the G W perspective, *Phys. Rev. B: Condens. Matter Mater. Phys.*, 2012, **86**(12), 125115.

105 N. Shahzad, A. Hussain, N. Mustafa, N. Ali, M. B. Kanoun and S. Goumri-Said, First principles study of the adsorption and dissociation mechanisms of H_2S on a TiO_2 anatase (001) surface, *RSC Adv.*, 2016, **6**(10), 7941–7949.

106 J. Hassan, S. Naz, A. Haider, A. Raza, A. Ul-Hamid, U. Qumar, J. Haider, S. Goumri-Said, M. B. Kanoun and M. Ikram, h-BN nanosheets doped with transition metals for environmental remediation; a DFT approach and molecular docking analysis, *Mater. Sci. Eng., B*, 2021, **272**, 115365.

107 S. Goumri-Said, M. Benali Kanoun, A. Manchon and U. Schwingenschlögl, Spin-polarization reversal at the interface between benzene and Fe (100), *J. Appl. Phys.*, 2013, **113**(1), 013905.